

The X-ray view of optically selected dual AGN

Alessandra De Rosa,¹★ Cristian Vignali^{2,3}, Paola Severgnini⁴, Stefano Bianchi⁵, Tamara Bogdanović⁶, Maria Charisi⁷, Matteo Guainazzi⁸, Zoltan Haiman⁹, S. Komossa¹⁰, Zsolt Paragi^{11,12}, Miguel Perez-Torres¹³, Enrico Piconcelli¹⁴, Lorenzo Ducci¹⁵, Manali Parvatikar¹⁵, Roberto Serafinelli¹

¹ INAF - Istituto di Astrofisica e Planetologia Spaziali (IAPS), via Fosso del Cavaliere, Roma, I-133, Italy

² Dipartimento di Fisica e Astronomia “Augusto Righi”, Università degli Studi di Bologna, Via Gobetti 93/2, 40129 Bologna, Italy

³ INAF - Osservatorio di Astrofisica e Scienza dello Spazio di Bologna, Via Gobetti 93/3, 40129 Bologna, Italy

⁴ INAF - Osservatorio Astronomico di Brera, via Brera 28, I-20121, Milano, Italy & via Bianchi 46, I-23807, Merate, Italy

⁵ Dipartimento di Matematica e Fisica, Università degli Studi Roma Tre, via della Vasca Navale 84, 00146 Roma, Italy

⁶ School of Physics and Center for Relativistic Astrophysics, Georgia Institute of Technology, Atlanta, GA 30332, USA

⁷ Department of Physics and Astronomy, Vanderbilt University, 2301 Vanderbilt Place, Nashville, TN 37235, USA

⁸ ESA - European Space Research and Technology Centre (ESTEC), Keplerlaan 1, 2201AZ Noordwijk, the Netherlands

⁹ Department of Astronomy, Columbia University, New York, NY, USA

¹⁰ Max-Planck-Institut für Radioastronomie, Auf dem Hügel 69, 53121 Bonn, Germany

¹¹ Department of Experimental Physics, University of Szeged, Dóm tér 9, H-6720 Szeged, Hungary

¹² Joint Institute for VLBI ERIC, Postbus 2, NL-7900 AA Dwingeloo, The Netherlands

¹³ Centro de Estudios de la Física del Cosmos de Aragón (CEFCA), 44001 Teruel, Spain

¹⁴ INAF - Osservatorio Astronomico di Roma, via Frascati 33, 00040 Monte Porzio Catone (Roma), Italy

¹⁵ Institut für Astronomie und Astrophysik, Kepler Center for Astro and Particle Physics, Universität Tübingen, Sand 1, 72076, Tübingen, Germany

Accepted XXX. Received YYY; in original form ZZZ

ABSTRACT

We present a study of optically selected dual AGN with projected separations of 3–97 kpc. Using multi-wavelength (MWL) information (optical, X-rays, mid-IR), we characterized the intrinsic nuclear properties of this sample and compared them with those of isolated systems. Among the 124 X-ray detected AGN candidates, 52 appear in pairs and 72 as single X-ray sources. Through MWL analysis, we confirmed the presence of the AGN in a fraction >80% of the detected targets in pairs (42 over 52). X-ray spectral analysis confirms the trend of increasing AGN luminosity with decreasing separation, suggesting that mergers may have contributed in triggering more luminous AGN. Through X/mid-IR ratio *vs* X-ray colors, we estimated a fraction of Compton-thin AGN (with $10^{22} \text{ cm}^{-2} < N_{\text{H}} < 10^{24} \text{ cm}^{-2}$) of about 80%, while about 16% are Compton thick (CT, with $N_{\text{H}} > 10^{24} \text{ cm}^{-2}$) sources. These fractions of obscured sources are larger than those found in samples of isolated AGN, confirming that pairs of AGN show higher obscuration. This trend is further confirmed by comparing the de-reddened [O III] emission with the observed X-ray luminosity. However, the derived fraction of Compton-thick sources in this sample at early stage of merging is lower than reported for late-merging dual-AGN samples. Comparing N_{H} from X-rays with that derived from E(B-V) from Narrow Line Regions, we find that the absorbing material is likely associated with the torus or the Broad Line Regions. We also explored the X-ray detection efficiency of dual-AGN candidates, finding that, when observed properly (at on-axis positions and with long exposures), X-ray data represent a powerful way to confirm and investigate dual-AGN systems.

Key words: galaxies: active – galaxies: Seyfert – galaxies: interactions – X-rays: general – infrared: galaxies

1 INTRODUCTION

Dual Active Galactic Nuclei (AGN), with separations of 100 pc–100 kpc, have been subject of interest due to their connection with Massive Black Holes (MBHs) triggering through mergers (Di Matteo et al. 2005; Treister et al. 2012) and as precursor of MBH coalescence (Amaro-Seoane et al. 2022, and reference therein). Dual AGN are hard to detect (see De Rosa et al. 2019 for a review on observational and theoretical aspects). Different techniques are used to select AGN pairs candidates in different wavebands (Burke-Spolaor 2011;

Comerford et al. 2012; Fu et al. 2015; Foord et al. 2020; Mannucci et al. 2022). Most published samples are sparse and not homogeneous and need to be confirmed through further multi-wavelengths (MWL) observational programs. Dual AGN at early stage of galaxies mergers (1–10 kpc scale) have been identified mostly serendipitously (Komossa et al. 2003; Ballo et al. 2004; Bianchi et al. 2008; Guainazzi et al. 2005; Piconcelli et al. 2010). Several studies have been performed at low redshift mainly through large surveys in optical, X-rays, IR (Koss et al. 2010; Comerford et al. 2012; Liu et al. 2011; Ricci et al. 2017). It has been also shown that higher luminosity AGN are found in interacting systems and average luminosity increases with decreasing separation (Hou et al. 2020; Satyapal et al.

★ E-mail: alessandra.derosa@inaf.it.

2014; Koss et al. 2012; Kocevski et al. 2012; Silverman et al. 2011), suggesting that mergers may trigger MBHs activity (Di Matteo et al. 2005; Treister et al. 2012). In this scenario of merger-triggered accretion, it is expected that MBHs are completely obscured by gas and dust during the final stage of merging (Hopkins et al. 2006).

Both cosmological and numerical simulations have investigated the dynamics and physics of merging MBHs, identifying several parameters that contribute in the activation of both MBHs at the same time (galaxy mass ratio, MBH orbital parameters) and the properties of the environment during the merger (Volonteri et al. 2022; Blecha et al. 2018; Capelo et al. 2017). Although observations have shown that AGN in mergers are characterized by higher obscuration with respect to isolated AGN (Ricci et al. 2021; Guainazzi et al. 2021; Pfeifle et al. 2019; De Rosa et al. 2018; Satyapal et al. 2017; Ricci et al. 2017; De Rosa et al. 2015; Kocevski et al. 2015), as expected from simulations, it still remains unclear how this obscuration evolves along the merger phase.

It is therefore fundamental to identify from theory and simulations the observational signatures to be compared with real observations and track the evolution of MBH through its coalescence. To make a step forward on this research, we need a statistically significant sample of dual AGN covering a wide dynamical range in spatial separations (1–100 kpc scale). SDSS offers a huge pool of optical data to extract good dual-AGN candidates through imaging (for spatially resolved systems) and spectroscopy (used for spatially unresolved systems), the so called double-peaked AGN (Wang et al. 2009; Ge et al. 2012; Smith et al. 2010; Kim et al. 2020). Double-peaked technique assumes that each AGN in the system carries its own Narrow Line Region (NLR) tracing the systemic velocity of the AGN as they move in their common gravitational potential. However, when the nature of the candidate is verified through MWL observations, only a tiny fraction of about 2% can be confirmed as dual AGN. This is due to the fact that the signature (i.e., the presence of a doubled-peaked profile) is not unique, indicating other possible effects originating nearby a single AGN (e.g., matter outflows); besides, the classification of a galaxy as an AGN is not easy due to extinction (Severgnini et al. 2012) and/or the presence of emission from star forming (SF) regions.

X-rays represent an efficient technique to detect and confirm accretion-dominated sources such as AGN, even in the case of moderate absorption (i.e. Compton-thin; column density $N_H \leq 10^{24} \text{ cm}^{-2}$). When used together with other diagnostics, e.g. mid-IR emission, even heavily obscured systems can be detected through their X-ray luminosity.

With the main objective of characterizing an homogeneous sample of dual AGN at kpc separation, and to compare their properties with isolated AGN, in this paper we present the X-ray study of a sample of optically selected dual AGN with separation in the range 3–97 kpc. We analysed the X-ray archival data from XMM-Newton and Chandra making use of targets selection in 4XMM (Webb et al. 2020) and CSC2 (Evans et al. 2020, 2010). The paper is structured as follows. In Sect. 2 we present the sample and its selection, while the MWL data analysis is presented in Sect. 3. The diagnostic tools used to identify AGN are shown in Sect. 4. We discuss our main results in Sect. 5 and provide a summary in Sect. 6. Throughout the paper we adopt a concordance cosmology with $H_0 = 70 \text{ km s}^{-1} \text{ Mpc}^{-1}$, $\Omega_\Lambda = 0.7$, $\Omega_M = 0.3$. Errors and upper limits quoted in the paper correspond to the 90 per cent confidence level, unless noted otherwise.

2 SAMPLE SELECTION

We considered the optically selected (SDSS) dual AGN by Liu et al. (2011), containing 2488 AGN in pairs (1244 systems at $\bar{z} \sim 0.1$ with line-of-sight velocity offsets $\Delta v < 600 \text{ km s}^{-1}$ and projected separations $< 100 h_{70}^{-1} \text{ kpc}$). Among these targets, 302 fall in the sky regions covered by XMM-Newton and/or Chandra (considering off-axis positions lower than $10'$ and $15'$ for Chandra and XMM-Newton, respectively, and exposure larger than 10 ks); the X-ray detection efficiency will be deeply investigated in the following Sect. 5.2. The optical catalogue was cross-correlated with 4XMM-DR10 (Webb et al. 2020) considering a match position in a circle with of $5''$ radius (which considers the XMM-Newton telescope position accuracy), obtaining 73 sources. Among these 73 sources, 37 appear as single AGN (7 over 37 with angular separation below $15''$) and 36 appear in pairs (hence, 18 dual-AGN systems). The main properties of the 18 AGN pairs are reported in the first block of Table 1. Due to the XMM-Newton spatial resolution and the redshift of the optical sample, the minimum projected separation we are able to explore is 7 kpc. In order to populate the sample with systems at closer separations, we performed the same selection using Chandra observations. We used the CSC2 catalogue (Evans et al. 2020, 2010), obtaining 51 additional targets with projected separation in the range 3–71 kpc. 16 CSC2 targets are in 8 pairs (see second block of Table 1), while 35 sources appear as single AGN. The spectral analysis of CSC2 targets has been reported in literature only for few sources. However, to include uniformity in the analysis, we re-analysed all of the sources. The final cross-match between optical and X-ray catalogues returns 124 targets (73 in 4XMM and 51 in CSC2): 52 of them appear in 26 dual systems with separations of 3.4–97.2 kpc (see Table 1). We noticed that the mean value and distribution of projected separations between the X-ray detected targets and the parent population from Liu et al. (2011) are in a good agreement (51 vs 58 kpc), although with a large dispersion (standard deviation of 30 kpc vs. 29 kpc).

For all detected targets, we also searched for mid-IR information. In this regard, the AllWISE catalog (Wright et al. 2010) provides the magnitudes in the Vega photometric system acquired in the four observational bands of WISE (W1=3.4 μm , W2=4.6 μm , W3=12 μm , W4=22 μm). To obtain flux densities, we used the conversion as in Jarrett et al. (2011), i.e., $F_\nu [\text{Jy}] = F_{\nu_0} \times 10^{-(m_{\text{Vega}}/2.5)}$, where F_{ν_0} is the zero magnitude flux density corresponding to the constant that gives the same response as that of Vega.

For 32 targets (4XMM: 17, CSC2: 15), we reached a sufficient signal-to-noise (S/N) ratio to enable X-ray spectral analysis. This threshold was choose of ~ 100 cts for 4XMM-EP8 in the band (0.2–12 keV), while in the case of Chandra we used the spectra released in CSC2 (see details in Evans et al. 2020). In the following section, we explore different diagnostics using a multi-wavelength approach in order to confirm the AGN nature for the 26 dual-AGN systems optically selected. The properties of the optically dual AGN detected as single X-ray sources will be investigated in a forthcoming paper (Parvatikar et al. in preparation).

We note that the dual AGN sample contains both, Seyfert galaxies (or quasars at higher luminosity) and low-ionization nuclear emission-line regions (LINERs), such that pairs are of the types Seyfert–Seyfert, Seyfert–LINER, and LINER–LINER. LINERs are known to be a mixed class of objects with diverse line excitation mechanisms discussed in the literature, such as old stars, shocks, halos of elliptical galaxies and even intra-cluster gas, as well as forms of AGN excitation (e.g. Heckman 1980; Shields 1992; Ho et al. 1993; Komossa et al. 1999). Therefore, not all LINERs are expected to be bona-fide AGN. Here, we continue to treat all LINERs as candidate

AGN, on a careful object-by-object basis including information from all optical emission lines. For sources that lie in the composite region of diagnostic diagrams (see Sect. 3.1) and in the LINER regime, we use the X-ray information to get further clues on the main power source of these systems and then re-assess their possible AGN nature in Sect. 4.

Finally, we would also like to note that the majority of the pairs in our sample are at large projected spatial separations, i.e. above $10''$ (see Table 1). Therefore, the well-known effect of light spillover into nearby fibers due to seeing, that can mimic AGN pairs when in fact only one of them is active (Husemann et al. 2020), is minimal in our sample.

3 SPECTRAL ANALYSIS

In this section, we present the MWL spectral analysis of our final sample comprising 26 dual AGN candidates (see Table 1). The main objective of this study is to confirm the nature of the selected targets and characterize their intrinsic properties such as X-ray luminosity, optical over X luminosity ratio and absorption properties (at nuclear and galaxy scale). As illustrated in Sect. 1, X-rays and mid-IR observations, along with optical spectroscopy, provide fundamental diagnostics to detect accreting MBHs even in heavily obscured systems, as expected in dual AGN.

3.1 Optical analysis

We retrieved the SDSS-III DR12 spectra (Alam et al. 2015) at the location of the dual-AGN systems, as reported in Table 1, from the survey webpage¹. The full-band optical spectra has been analysed through the software package QSFIT 1.3.0 (Calderone et al. 2017). This tool automatically takes into account the emission from both AGN and host galaxy, along with a number of broad and narrow emission lines. In particular, we extracted the intensities of the primary diagnostic narrow emission lines such as H β , [OIII] λ 5007, [OI] λ 6300, H α , [NII] λ 6583 and [SII] λ 6717, 6730. Line fluxes were corrected for Galaxy extinction using NED database². The line flux ratios were then plotted in the diagnostic diagrams (Kauffmann et al. 2003, BPT diagram) shown in Fig. 1 (upper panels refers to XMM-Newton sources and bottom panels to Chandra sources), where the regions populated with Seyfert galaxies, SF galaxies, and LINERs are identified as in Kewley et al. (2006). Each number in the plot refers to sources in Table 1; same colors refer to members of a pair. Some of the optical spectra are dominated by galaxy contribution, however when possible we also evaluated the extinction E(B-V) considering the Balmer decrement from the narrow emission lines. Sources with at least one BPT diagram indicating an AGN or LINER are included in our sample. There are, however, targets whose optical analysis does not confirm their AGN nature. We kept these sources in the catalogue and will investigate their classification using further diagnostics such as the X-ray luminosity and mid-IR vs X-ray colors in Sect. 4. We note that only two sources show clear evidence of broad optical lines (J094554.4+423840 and J103853.2+392151, De Rosa et al. 2018), while in the rest of the sample the galaxy contribution prevent us to detect any strong broad-line component.

3.2 X-ray analysis

We reduced XMM-Newton data using SAS software V17.0 with standard settings and the most updated calibration files available at the time of the data reduction. Period of high and flaring background were removed applying appropriate threshold on single events extracted above 10 keV (about 0.4 and 0.35 counts per second in EPIC-pn and EPIC-MOS, respectively).

Depending on the source counts and the separation of the two sources in each system, we extracted EPIC spectra from circular regions with radii in the range $11''$ – $25''$; these regions include ~ 60 – 90% of the source counts at 1.5 keV in the EPIC cameras. Background spectra were extracted in the same CCD chip using circular regions free from contaminating sources. Due to the higher net counts in the 0.3–10 keV energy band with respect to EPIC/MOS, we reported the EPIC/pn spectra analysis and checked a posteriori that pn+MOS data do not improve the fit neither the spectral parameter constraints. Chandra spectra and corresponding response matrices were retrieved from CSC2. When multiple observations of the same source were available, we verified the absence of any sign of variability and the spectra from the individual observations were merged to increase the S/N ratio (the ObsID for each observation is reported in Table 1).

Among the 52 sources, we were able to extract spectral information for 32 targets (4XMM: 17, CSC2: 15). For these sources, EPIC-pn and ACIS background-subtracted spectra were fitted with the software xspec v12.10 Arnaud (1996) using Cash statistics (Cash 1979; Wachter et al. 1979). We applied a phenomenological model composed of (1) an absorbed power-law; this is the nuclear emission due to Comptonization of electrons in a hot corona by seed photons, probably originated in the accretion disc (e.g. Haardt & Maraschi 1993; Haardt et al. 1994), (2) a soft, unabsorbed power-law component reproducing the extended soft X-ray emission below ~ 2 keV, likely associated with the NLR (Bianchi et al. 2019, and references therein), scattering of the primary emission (Ueda et al. 2007), or to star-formation activity (Ranalli et al. 2003). The baseline model can be written as $e^{-N_H^{\text{Gal}}\sigma} (e^{-N_H\sigma} K_h E^{-\Gamma_h} + K_s E^{-\Gamma_s})$, where Γ_h and Γ_s are the photon indices of the nuclear primary component and soft X-ray component, respectively; N_H^{Gal} is the Galactic column density, N_H the cold absorption column density at the redshift of the source; σ is the photo-absorption cross-section from Balucinska-Church & McCammon (1992). This simple model is sufficient to get constraints on the main spectral parameters of interest, such as N_H^Z , Γ and the unabsorbed luminosity.

If count statistic does not allow us to constrain simultaneously Γ_h and Γ_s , we put $\Gamma_h = \Gamma_s$, as expected in a scattering model for the soft excess discussed above. We also fixed Γ_h to a typical value of 1.9 (Ricci et al. 2017) when counts statistic does not allow to fit the parameter. The results of the spectral analysis and modeling performed on the sample are reported in Table 2.

4 AGN IDENTIFICATION

We used different diagnostics in order to confirm the AGN nature of our sample against SF galaxies that could produce the observed X-ray luminosity.

We anticipate that, at the end of our MWL analysis, we selected 42 confirmed AGN among 52 candidates. For 24 of these AGN we could perform a detailed X-ray spectral modeling as described in Sect. 3.2. This "clean sample" of 24 AGN has been then used to calibrate MWL relations in order to get information on the nature

¹ <http://skyserver.sdss3.org/>

² <https://ned.ipac.caltech.edu/Documents/References/ExtinctionCalculators>

Table 1. Dual-AGN candidates detected in 4XMM-XMM-Newton and CSC2. Numbering in the first column refers to sources shown in Fig. 1. Sources in *italic* are not identified as AGN following our diagnostic (see Sect. 4).

	ObsID	SimbadName (SDSS)	RA (deg)	DEC (deg)	z	⁽¹⁾ sep (arcsec)	⁽²⁾ rp (kpc)	IAUNAME (4XMM/2CXO)	⁽³⁾ Net counts (counts)	ref
XMM-Newton										
1	0761730401	J015235.35-083236.6	28.14729	-8.5435	0.0517	58.5	58.9	J015235.2-083233	73±13	
2	0761730401	J015235.99-083138.9	28.14996	-8.52747	0.0511	58.5	58.9	J015235.9-083139	69±12	
3	0741580501	J082321.66+042220.9	125.84029	4.37247	0.0311	142.8	88.7	J082321.6+042221	8871±125	H20
4	0741580501	J082329.87+042332.9	125.8745	4.3925	0.0308	142.8	88.7	J082329.9+042332	39±10	H20
5	0740620201	J083157.64+191241.4	127.99021	19.21153	0.0372	55.8	41.2	J083157.6+191241	149±21	
6	0740620201	J083200.51+191205.8	128.00212	19.20164	0.0375	55.8	41.2	J083200.6+191206	86±13	
7	0743110701	J100133.68+033731.1	150.39033	3.62533	0.0437	53.8	45.3	J100133.4+033731	314±48	
8	0743110701	J100135.80+033647.8	150.39921	3.61328	0.0427	53.8	45.3	J100135.8+033648	260±29	
9	0503600301	J100230.89+324252.3	150.62871	32.71456	0.049	89.3	88.1	J100230.8+324248	71±15	
10	0503600301	J100236.54+324224.2	150.65225	32.70675	0.0505	89.3	88.1	J100236.6+324224	2359±93	
11	0146990101	J102141.89+130550.3	155.42454	13.09733	0.0765	67.1	97.2	J102141.8+130551	45±11	H20
12	0146990101	<i>‡J102142.78+130656.1</i>	155.42829	13.11558	0.0763	67.1	97.2	J102142.6+130654	179±17	H20
13	0692330501	<i>‡J112545.04+144035.6</i>	171.43771	14.67658	0.034	73.6	49.7	J112545.1+144035	622±30	H20, TA18
14	0692330501	J112549.54+144006.5	171.45646	14.6685	0.0339	73.6	49.7	J112549.5+144006	249±21	H20, TA18
15	0555060501	J120157.72+295926.6	180.4905	29.99075	0.072	19.1	25.9	J120157.8+295927	62±11	
16	0555060501	J120157.88+295945.5	180.49117	29.996	0.0713	19.1	25.9	J120157.8+295945	40±10	
17	0601780601	J120443.31+311038.2	181.1805	31.17728	0.025	61.5	31.0	J120443.3+311037	16517±137	K10
18	0601780601	J120445.19+311132.9	181.18833	31.19247	0.025	61.5	31.0	J120445.3+311130	154±20	K10
19	0111281601	J134130.40-002514.3	205.37671	-0.42072	0.0713	61.5	83.6	J134130.5-002512	30±9	
20	0111281601	J134133.37-002432.0	205.38904	-0.40892	0.0719	61.5	83.6	J134133.4-002431	42±9	
21	0783520501	J145627.39+211955.9	224.11417	21.33222	0.0443	68.4	59.2	J145627.4+211956	[†] 602±25	ADR18
22	0783520501	J145631.35+212030.0	224.13067	21.34169	0.044	68.4	59.2	J145631.3+212030	[†] 459±32	ADR18
23	0721820201	J145838.58+382727.9	224.66075	38.45775	0.1358	32.6	78.8	J145838.5+382727	124±16	
24	0721820201	J145840.73+382732.7	224.66971	38.45908	0.1367	32.6	78.8	J145840.6+382730	73±16	
25	0147210301	J160501.37+174632.4	241.25571	17.77569	0.033	117.3	78.1	J160501.3+174632	77±14	H20,
26	0147210301	J160507.88+174527.6	241.28287	17.75767	0.0334	117.3	78.1	J160508.1+174528	109±27	H20,
27	0783520301	J162640.93+142243.6	246.67054	14.37878	0.0479	54.1	51.3	J162640.9+142243	[†] 364±20	ADR18
28	0783520301	J162644.50+142250.6	246.68546	14.38075	0.0484	54.1	51.3	J162644.4+142253	[†] 162±15	ADR18
29	0784521201	J163102.72+394733.0	247.76133	39.7925	0.0289	165.8	96.0	J163102.7+394733	345±28	
30	0784521201	J163103.40+395018.5	247.76421	39.83847	0.0305	165.8	96.0	J163103.4+395015	85±17	
31	0673000147	J221839.91-002402.0	334.66633	-0.40053	0.0948	30.7	54.2	J221839.8-002400	38±10	
32	0673000147	<i>‡J221840.97-002335.5</i>	334.67071	-0.39319	0.095	30.7	54.2	J221840.9-002333	20±8	
33	0783520101	J094554.40+423839.9	146.47671	42.6444	0.0745	21.3	30.3	J094554.4+423839	[†] 21450±150	ADR18
34	0783520101	J094554.49+423818.7	146.47701	42.6385	0.0745	21.3	30.3	J094554.4+423839	[†] 1275±37	ADR18
35	0783520201	J103853.29+392151.1	159.72204	39.36422	0.0548	40.4	42.9	J103853.3+392151	[†] 6534±80	ADR18
36	0783520201	J103855.94+392157.5	159.73312	39.36660	0.0548	40.4	42.9	J103855.9+392157	[†] 182±14	ADR18
Chandra										
1	14965	J090714.44+520343.4	136.81021	52.06206	0.0596	7.6	8.9	J090714.4+520343	41.9 ^{+7.2} _{-6.5}	H19,H20
2	14965	J090714.61+520350.6	136.81087	52.06408	0.0602	7.6	8.9	J090714.6+520350	120.9 ^{+11.6} _{-11.5}	H19,H20
3	4110, 4934	J121345.92+024838.9	183.44146	2.81083	0.073	3.4	4.8	J121345.9+024838	11.3 ^{+4.1} _{-3.4}	H20,I11,R21
4	4110, 4934	J121346.07+024841.4	183.44212	2.8115	0.0731	3.4	4.8	J121346.0+024841	14.9 ^{+4.5} _{-3.9}	H20,I11,R21
5	2043	<i>‡J124610.10+304354.9</i>	191.54212	30.73192	0.0219	37.2	16.4	J124610.0+304355	18.3 ^{+5.4} _{-4.7}	H20
6	2043	J124611.24+304321.8	191.54683	30.72275	0.0218	37.2	16.4	J124611.2+304321	70.6 ^{+9.0} _{-9.0}	H20
7	♣	<i>‡J125929.96+275723.1</i>	194.87483	27.95644	0.0227	71.3	34.4	J125929.9+275723	154.2 ^{+31.3} _{-31.5}	H20
8	♣	<i>‡J125934.12+275648.6</i>	194.89217	27.94683	0.024	71.3	34.4	J125934.1+275648	334.7 ^{+30.3} _{-30.2}	H20
9	12242	<i>‡J131513.87+442426.4</i>	198.80779	44.40736	0.0354	50.9	35.9	J131513.8+442426	14.5 ^{+4.5} _{-3.9}	H20
10	12242	J131517.26+442425.5	198.82196	44.40711	0.0355	50.9	35.9	J131517.3+442425	3835.5 ^{+65.4} _{-64.8}	H20
11	2044	J133817.27+481632.1	204.57196	48.27564	0.0278	11.5	6.4	J133817.3+481632	95.2 ^{+10.6} _{-10.6}	Ma12,H20,I20
12	2044	J133817.77+481640.9	204.57404	48.27808	0.0277	11.5	6.4	J133817.8+481640	205.0 ^{+15.2} _{-15.2}	Ma12,H20,I20
13	11845	<i>‡J150457.12+260058.4</i>	226.238	26.01625	0.054	61.6	65.2	J150457.1+260058	68.0 ^{+9.5} _{-9.4}	H20
14	11845	<i>‡J150501.22+260101.5</i>	226.25508	26.01708	0.0545	61.6	65.2	J150501.2+260101	15.1 ^{+4.6} _{-4.0}	H20
15	14968	<i>‡J154403.45+044607.5</i>	236.01437	4.76875	0.042	4.1	3.4	J154403.4+044607	5.0 ^{+2.9} _{-2.2}	H19,H20
16	14968	J154403.66+044610.0	236.01529	4.76947	0.0416	4.1	3.4	J154403.6+044609	59.3 ^{+8.2} _{-8.1}	H19,H20

⁽¹⁾–⁽²⁾ Angular and projected separation between the sources; ⁽³⁾ Net observed count in (0.2–12 keV) for 4XMM (EP8) and (2–8 keV) for CSC; ⁽⁴⁾References: H19: Hou et al. 2019; H20: Hou et al. 2020; K10: Koss et al. 2010; ADR18: De Rosa et al. 2018; I20: Iwasawa et al. 2020; MA12: Mazzarella et al. 2012; R21: Ricci et al. 2021; I11: Iwasawa et al. 2011; TA18: Torres-Albà et al. 2018. [†] For these sources we report here the values obtained in De Rosa et al. 2018. ♣ ObsID=9714, 10672, 13993, 13994, 13995, 13996, 14406, 14410, 14411, 14415.

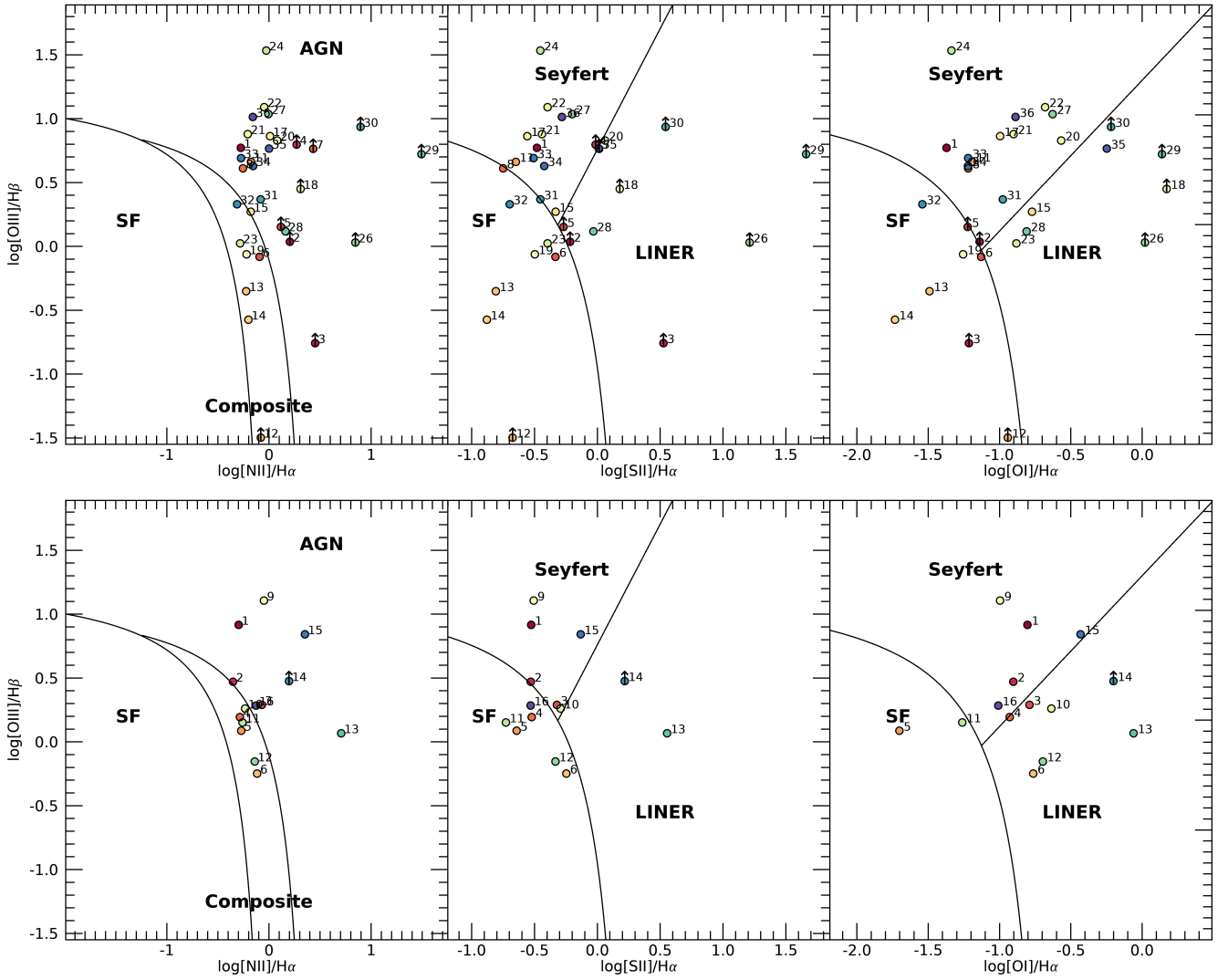


Figure 1. Optical emission-line ratios as classical diagnostic plot for identification of dual-AGN candidates detected in 4XMM (upper panels) and CSC2 (lower panels). Same color refers to members of the same pair. Number of each source refer to Table 1. AGN, LINER and SF regions in the plots are separated according to Kewley et al. (2006).

(AGN, no-AGN) and absorption properties of the whole sample of 42 dual AGN. Below we report the details of this study.

As anticipated in the previous section, we retain in the sample targets indicating the presence of an AGN or LINER in at least one optical BPT diagram (see Fig. 1). The X-ray luminosity of the sources associated to LINER through optical analysis suggests that their emission is powered by the AGN (see Table 2). In fact, a systematic study of a large sample of LINERs identified as unresolved sources at high X-ray energies (4.5–8 keV) suggested that AGN-like objects tend to have higher 2–10 keV luminosity than non-AGN objects, with average values $\log L_X/(\text{erg s}^{-1}) \sim 41$ and $\log L_X/(\text{erg s}^{-1}) \sim 39$, respectively (González-Martín et al. 2009). As a further check to firmly identify AGN, we used the X-ray/mid-IR vs X-ray colors relation.

In Figure 2 (left panel) we show the absorption column density vs hardness ratio HR ($\text{HR}=(\text{H}-\text{S})/(\text{H}+\text{S})$, where H and S are the source counts in the soft and hard energy bands), for the 24 sources with spectral information. The hardness ratio HR is evaluated using

$\text{S}=2\text{--}4.5$ keV and $\text{H}=4.5\text{--}10$ keV energy bands for XMM-Newton and $\text{S}=0.5\text{--}2$ keV $\text{H}=2\text{--}8$ keV for Chandra. Sources with larger obscuration are characterized by larger HR. In particular, in our clean sample, a value of HR larger than about -0.3 indicates a $N_H \gtrsim 10^{22} \text{ cm}^{-2}$ (see Fig. 2, left).

Mid-IR emission in AGN is thought to originate within the dusty torus reprocessing the optical-UV primary emission (Padovani et al. 2017, and references therein), and mid-IR color-color diagrams offer important diagnostic in order to identify AGN candidates. Using classical color-color diagrams through WISE 3-bands measurements ($[2.4\text{--}4.6] \mu\text{m}$ vs $[4.6\text{--}12] \mu\text{m}$, (Mateos et al. 2012; Assef et al. 2013; Yan et al. 2013), our candidates roughly lie the AGN region ($[4.6\text{--}12] \mu\text{m}$ above 2) and tend toward red colors ($[2.4\text{--}4.6] \mu\text{m}$ above 0.3), as suggested for AGN in mergers (Satyapal et al. 2014; Weston et al. 2017). Nevertheless, AGN are not the largest population in mid-IR surveys, which are dominated by strong IR emission from SF and normal galaxies. This is the reason why combined mid-IR

and X-rays analysis provides further information to confirm AGN candidates (Severgnini et al. 2012; Terashima et al. 2015).

Severgnini et al. (2012) proposed an effective technique to classify AGN and SF galaxies by comparing mid-IR (12–25 μm) and X-ray fluxes. In their diagnostic plot, the X-ray/mid-IR flux ratio is compared with the X-ray hardness ratio values, identifying different regions in the plot where different populations (SF galaxies, unobscured AGN, Compton-thin AGN and Compton-thick AGN) are clustered. Then we use the ratio $F(\text{X-rays})/F(22\ \mu\text{m})$ vs HR relation reported in the right panel of Fig. 2 to exclude X-ray detected targets which are not associated with AGN and evaluate (in Sect. 5.1) the level of absorption for the sources in the total sample without X-ray spectral information (see Table 1 and Fig. 2, right panel). Using the results of spectral analysis for the sources with enough counts (our “clean” sample), we calibrated the X/mid-IR vs HR plot that allowed also to identify the regions where different types of emitters are expected (details will be presented in Sect. 5.1): we choose the limit $\text{HR} > -0.3$ (as obtained for obscured sources with $N_{\text{H}} \gtrsim 10^{22}\ \text{cm}^{-2}$) and, as X/IR ratio, we adopted a threshold of 0.01 (blue dash-dotted lines in Fig. 2). We note that, given the intrinsic dispersion of the X/mid-IR vs HR relation, these values are not different from those adopted by Severgnini et al. (2012).

Using optical classification (see Fig. 1) and X-ray/mid-IR ratio (see Fig. 2, right), we identified and confirmed 42 AGN (4XMM: 33 targets and CSC2: 9 targets), which is 80% of the detected targets in pairs (52). The last two columns in Table 2 report the classification of each source as obtained with Optical and X-ray/mid-IR ratio. The sources that did not pass at least one of the two checks are indicated in italic in Table 1 and Table 2; however, when available, we report the results of their X-ray spectral fit for completeness. A peculiar but illustrative case is J133817.3+481632 (aka Arp 266) which is a known Compton-thick AGN hosted in a dual system (Iwasawa et al. 2020; Mazzarella et al. 2012). It appears as a SF galaxy in our X-ray/mid-IR diagnostic plot and BPT (see src # 11 in Fig. 1, lower panel), suggesting that the number of heavily absorbed AGN in our final sample should be consider a lower-limit (see further discussion in Sect. 5.2). A similar case of such highly obscured system is NGC 6240 (Komossa et al. 2003).

We also note that, for pair candidates detected by *Chandra* (see Table 1), four are at angular separation below $12''$ which corresponds to the WISE 22 μm resolution (Wright et al. 2010). One of these four systems is the well known AGN pair Arp 266 that we have just discussed. However, considering the X/mid-IR vs HR diagnostic plot, the decrease of the IR flux (due to blended emission between the two sources) will move the sources in the AGN region, resulting, once again, in a lower-limit in our estimated AGN fraction in the final sample.

Table 2. X-ray properties of our clean sample of dual AGN sources detected with *XMM-Newton* and *Chandra*. Sources in [‡]*italic* did not pass the check for AGN classification.

IAUNAME (4XMM/2CXO)	(1) $N_{\text{H}}^{\text{Gal}}$ (10^{20} cm^{-2})	(2) N_{H} (10^{22} cm^{-2})	(3) Γ_{h}	(4) $F_{\text{X}}^{\text{Obs}}$ ($10^{-14} \text{ erg cm}^{-2} \text{ s}^{-1}$)	(5) $L_{\text{X}}^{\text{Una}}$ ($10^{40} \text{ erg s}^{-1}$)	(6) $L_{[\text{OIII}]}^{\text{corr}}$ ($10^{40} \text{ erg s}^{-1}$)	(7) W4 (mag)	(8) E(B-V) (mag)	(9) (X/IR)	(10) Opt
XMM-Newton										
J082321.6+042221	2.5	$0.6^{+1.4}_{-0.3}$	$3.03^{+0.50}_{-0.44}$	$10.^{+1}_{-1}$	22^{+4}_{-8}	>0.015	8.4	-	U	A
J100135.8+033648	1.9	16^{+31}_{-10}	1.9^{\star}	$6.3^{+1.1}_{-1.1}$	46^{+15}_{-15}	21.5	6.45 ± 0.05	0.70	t	A
J100236.6+324224	1.3	< 0.4	$2.2^{+0.9}_{-0.6}$	10^{+1}_{-1}	47^{+10}_{-10}	-	8.35	-	U	C
[‡] <i>J102142.6+130654</i>	4.3	< 0.06	1.9^{\star}	0.8 ± 0.4	10 ± 4	>0.06	4.34 ± 0.04	-	SF	SF
[‡] <i>J112545.1+144035</i>	2.5	$0.2^{+0.4}_{-0.1}$	1.9^{\star}	$1.2^{+0.2}_{-0.2}$	3.3 ± 1.0	13.6	3.66 ± 0.02	1.3	SF	C
J112549.5+144006	2.4	12^{+55}_{-8}	1.9^{\star}	1.6 ± 0.3	8.0 ± 0.4	6.3	4.44 ± 0.03	1.3	T	C
J120443.3+311037	1.4	3.7 ± 0.5	1.7 ± 0.4	263 ± 6	309 ± 5	43	3.59 ± 0.02	1.43	t	A
J120445.3+311130	0.44	24^{+150}_{-12}	1.9^{\star}	$3.0^{+1.1}_{-1.1}$	11^{+7}_{-6}	>0.2	7.92 ± 0.15	-	T	A
J145627.4+211956	2.9	75^{+28}_{-23}	1.9 ± 0.9	$8.6^{+2.0}_{-2.0}$	370^{+20}_{-130}	> 4.5	7.15 ± 0.08	0.35	t	A
J145631.3+212030	2.9	> 100	1.9^{\star}	$2.3^{+0.5}_{-0.5}$	700^{\dagger}	39	5.32 ± 0.03	0.54	T	A
J145838.5+382727	1.2	< 0.6	1.9^{\star}	$1.2^{+0.2}_{-0.2}$	60 ± 20	46.8	7.34 ± 0.08	0.63	t	A
J162640.9+142243	3.8	67^{+150}_{-50}	1.9^{\star}	2.3^{+1}_{-1}	80^{+30}_{-70}	31	5.54 ± 0.11	0.44	T	A
J162644.4+142253	3.8	6^{+12}_{-4}	1.9^{\star}	1.6 ± 0.8	12 ± 0.8	> 0.1	9.04 ± 0.53	-	t	A
J094554.4+423840	1.1	< 0.02	2.4 ± 0.1	50 ± 3	700 ± 30	27.9	5.45 ± 0.04	0.40	U	A
J094554.4+423818	1.1	24^{+8}_{-6}	1.9^{\star}	19 ± 2	690 ± 30	124	5.84 ± 0.05	0.55	t	A
J103853.2+392151	1.7	< 0.03	1.62 ± 0.07	55 ± 5	420 ± 20	8.0	7.66 ± 0.14	0.33	U	A
J103855.9+392157	1.7	> 100	1.9^{\star}	1.6 ± 1	700^{\dagger}	19	6.05 ± 0.05	0.30	SF	A
Chandra										
J090714.4+520343	1.5	18^{+16}_{-12}	1.9^{\star}	6.4 ± 1.1	160 ± 30	104	6.8 ± 0.1	1.11	t	A
J090714.6+520350	1.5	$2.5^{+1.4}_{-1.1}$	1.5 ± 0.7	13 ± 1	160 ± 1	38	6.8 ± 0.1	0.85	t	A
J121345.9+024838	1.7	<0.56	1.9^{\star}	$0.7^{+0.2}_{-0.2}$	11 ± 4	46	3.61 ± 0.02	1.48	T/SF	L
J121346.0+024841	1.7	-	2.1 ± 0.6	0.9 ± 0.2	13 ± 3	80	3.61 ± 0.02	1.17	SF	C
[‡] <i>J124610.0+304355</i>	1.16	$0.16^{+0.1}_{-0.8}$	1.9^{\star}	1.1 ± 0.5	1.4 ± 0.1	5.3	4.08 ± 0.03	1.37	SF	SF
J124611.2+304321	1.16	$0.17^{+0.1}_{-0.1}$	1.9^{\star}	1.2 ± 0.3	1.5 ± 0.1	0.5	7.4 ± 0.1	0.43	U	C/L
<i>J125934.1+275648</i>	0.9	-	$1.7^{+0.9}_{-0.1}$	<0.67	<1	8.4	-	-	-	-
<i>J131513.8+442426</i>	1.7	-	$3.0^{+1.3}_{-1.1}$	0.055	<0.18	150	6.19 ± 0.05	1.57	SF	A
J131517.3+442425	1.7	$9.5^{+0.5}_{-0.4}$	1.9^{\star}	330 ± 5	$(1.9^{+2.1}_{-0.8}) \times 10^3$	59	3.43 ± 0.02	0.83	t	C
J133817.3+481632	1.4	>200	1.6 ± 0.3	2.2 ± 0.9	$(1.3^{+2.7}_{-0.8}) \times 10^3$	13.8	2.54 ± 0.01	0.71	SF	C/SF
J133817.8+481640	1.4	6.8 ± 3.8	1.9^{\star}	24.6 ± 2.0	40.	14.9	2.54 ± 0.01	-	t	C/SF
[‡] <i>J150457.1+260058</i>	3.5	-	1.9^{\star}	0.2 ± 0.1	1.5 ± 0.2	0.06	8.8 ± 0.1	-	SF	Amb
[‡] <i>J150501.2+260101</i>	3.5	-	$1.1^{+0.9}_{-0.7}$	<0.1	<0.9	0.08	8.8 ± 0.1	-	SF	Amb
[‡] <i>J154403.4+044607</i>	3.9	-	$2.9^{+1.2}_{-1.1}$	<0.1	<0.46	150	6.38 ± 0.07	2	SF	L
J154403.6+044609	3.9	$2.8^{+2.8}_{-1.9}$	$1.3^{+1.2}_{-1.0}$	8.1 ± 0.9	48 ± 9	25	6.38 ± 0.07	1.2	t	L

(¹) Galactic column density of NI from [HI4PI Collaboration et al. 2016](#); (²) Nuclear absorption column density. "-" refers to source with upper limit on N_{H} of fews 10^{20} cm^{-2} ; (³) Photon index of the hard power-law; values with \star are left fixed in the fit; (⁴) Observed 0.5–10 keV (4XMM) and 2–8 keV (2CXO) X-ray flux in $10^{-14} \text{ erg cm}^{-2} \text{ s}^{-1}$; (⁵) Unobscured 2–10 keV X-ray Luminosity in $10^{40} \text{ erg s}^{-1}$; \dagger For Compton-thick sources, we used the relation in [Lamastra et al. \(2009\)](#); [Marinucci et al. \(2012\)](#): the intrinsic 2–10 keV luminosity has been obtained by multiplying the observed luminosity by 70; (⁶) De-reddened [OIII] luminosity in $10^{40} \text{ erg s}^{-1}$; (⁷) WISE W4 magnitude.; (⁸) Extinction considering the Balmer decrement from narrow emission lines. "-" indicates sources where precise measure of $H\beta$ has not been obtained (see Sect. 3.1 for details); (^{9–10}) Source classification following the X/IR vs HR and Optical diagnostics. A: AGN, SF: Star-Forming, L: Liner, C: Composite, U: Unabsorbed, t: Compton thin, T: Compton Thick, Amb: Ambiguous.

5 DISCUSSION

5.1 Absorption properties

We were able to extract X-ray spectra and perform a detailed analysis for 32 sources among the 52 AGN candidates in 4XMM and CSC2. The optical and X-ray/mid-IR presented in Sect. 4 points towards an AGN classification for 24 out of 32 targets. We present the spectral analysis for all 32 sources with best-fit values in Table 2; however, we excluded from our final considerations on dual-AGN properties all sources (8) which are not confirmed as AGN (reported in italic in Table 2).

In the left panel of Figure 3, we plot the intrinsic unobscured X-ray luminosity of our dual-AGN sample with spectral information in bins of projected separation r_p . A trend of increasing luminosity with decreasing r_p is suggested, although it should be considered that the bin $r_p > 60$ kpc is poorly populated (3 AGN) in this analysis, while smaller separation bins are populated with 10 (0–30 kpc) and 11 (30–60 kpc) targets.

Among the 24 targets with measured N_H , a fraction of 70–74% exhibits an absorption column density larger than 10^{22} cm^{-2} at 3–100 kpc separation (see the right panel in Figure 3). We measure an upper limit $N_H < 3 \times 10^{22} \text{ cm}^{-2}$ for the two AGN showing broad optical emission lines (J094554.4+423840 and J103853.2+392151, De Rosa et al. 2018 see Sect. 3.1). Although we do not see a clear trend of absorption with r_p (but see further discussion below based on the absorption on the whole sample), we note that there are not absorbed AGN ($N_H < 10^{22} \text{ cm}^{-2}$) in systems with projected separation above 60 kpc. The fraction of absorbed AGN in dual systems is larger than that measured in samples of isolated AGN (e.g., 45% in BAT, Ricci et al. 2015), which is in agreement with previous studies on X-ray dual AGN (Koss et al. 2011; De Rosa et al. 2018; Ricci et al. 2017, 2021). However, we note here that our sample is neither complete nor unbiased in any sense. In order to evaluate the amount of absorption in the 42 X-ray dual AGN, we use indirect measurements. Below we describe two main proxies for absorption: [OIII]/X ratio, IR/X ratio vs hardness ratio.

5.1.1 L_X vs $L_{\text{[OIII]}}$

Once that extinction within the NLR is properly considered, the luminosity of the emission line from [OIII] $\lambda 5007$ may be used as a good indicator of the intrinsic luminosity of the source. In our analysis of optical spectra (Sect. 3.1), we correct the [O III] emission for the extinction through the Balmer decrement ($H\alpha/H\beta$ ratio). To derive the $L_{\text{[OIII]}}^{\text{corr}}$ corrected for extinction, we used the relation from Bassani et al. (1999) which assumes the Cardelli et al. (1989) extinction law and an intrinsic Balmer decrement equal to 3; this value represents the case for the NLR (Osterbrock & Ferland 2006). Value of $L_{\text{[OIII]}}^{\text{corr}}$ for the sources with X-ray spectral information are reported in Table 2. The ratio between the observed X-ray luminosity and the $L_{\text{[OIII]}}^{\text{corr}}$ has been therefore used as an indirect measurement of N_H . The $L_X/L_{\text{[OIII]}}^{\text{corr}}$ relation has been deeply analysed in large samples of type 1 and type 2 AGN (Heckman et al. 2005; Mulchaey et al. 1994; Bassani et al. 1999; Lamastra et al. 2009; Vignali et al. 2010), and empirical trends have been found by several authors.

In fig. 4 we report the observed X-ray luminosity vs the [O III] luminosity corrected for extinction $L_{\text{[OIII]}}^{\text{corr}}$. For the sources without a measure of $H\beta$ emission, we considered the observed value of [O III] that should be then regarded as a lower limit to $L_{\text{[OIII]}}^{\text{corr}}$. As comparison, we also plot the relation found by Lamastra et al. (2009)

for a sample of Compton-thin AGN. Almost 80% of our sample lies below the threshold as defined in Lamastra et al. (2009), clearly showing that our sources exhibit excess of absorption with respect to what is expected in isolated Compton-thin AGN. In the X-[O III] plane, the two type 1 AGN in our sample (094554.4+423840 and J103853.2+392151) are both located above the relation defined for obscured sources, as expected.

With the caveat that for some sources of the sample only a lower limit to the $H\beta$ emission has been obtained, we can compare the column density derived from the E(B-V) – evaluated from the NLR (see Table 2, Domínguez et al. 2013) and using, for the conversion, the Galactic $N_H/E(B-V)$ ratio (Draine 2011) – with the N_H measured from the X-ray analysis (excluding type 1 AGN). The extinction in the NLR is lower than the obscuration derived from X-rays, and there is no evidence for a trend of increasing E(B-V) as a function of the separation r_p as observed for X-ray derived N_H in Fig. 3 (right panel). This result suggests that the gas responsible for the X-ray obscuration is likely associated with the torus and/or the BLR (e.g., Padovani et al. 2017).

5.1.2 $F_X/F_{\text{[IR]}}$ vs X-ray hardness ratio

As anticipated in Sect. 4, we used mid-IR/X-ray flux ratio to identify the AGN among the X-ray detected targets (see Table 1). This ratio, when compared with X-ray colors, provides a powerful diagnostic for obscuration (Severgnini et al. 2012), also when N_H is not available from X-ray fitting procedures. We then use the clean sample with spectral information (24 AGN, see Table 2) to calibrate the N_H vs HR relation to be used in the total sample, as discussed in Sect. 4 and shown in Fig. 2 left panel.

The plot X/mid-IR vs HR in Fig. 2 right allow us to identify four regions for unabsorbed, SF galaxies, Compton-thin and Compton-thick (CT) sources. The sources in the bottom-left block are identified as star-forming galaxies also from optical analysis (see Sect. 3.1 and Fig. 1). We checked that, within the diagnostic plot, all sources analysed through X-rays and optical analysis are correctly located: in Table 2 we report the identification obtained with all diagnostic, X-rays, optical and X/MIR vs HR. We, however, noted that J133817.3+481632 (a.k.a. Arp 266 SW) and J103855.9+392157, which are Compton thick, fall in the SF region, being their spectra dominated by the soft X-ray component with the nuclear emission completely obscured (Iwasawa et al. 2020; De Rosa et al. 2018). This is also in agreement, as anticipated in Sect. 4, with the optical classification of these targets, yet demonstrating that we can miss a number of Compton-thick sources in our final sample of confirmed AGN.

If we consider all 42 confirmed AGN detected in 4XMM (33) and CSC (9) in fig. 2 (right panel), the mid-IR and X-ray diagnostic suggests that our sample is composed of 80% Compton-thin AGN, 16% CT and 4% unobscured sources. As mentioned above, the number of CT sources can be regarded as a lower-limit. If we compare these fractions to isolated AGN, we confirm the trend of more obscured AGN hosted in pairs. As pointed out above, we do not see a clear trend of increasing N_H with decreasing r_p (see Fig. 3, left). However, the fraction of absorbed AGN in these dual-AGN systems that are in early stages of merger (projected separation up to 100 kpc) is lower with respect to the fraction of heavily obscured AGN found in systems in late stages of merging (e.g. Ricci et al. 2021), suggesting the presence of larger reservoir of nuclear gas or with a different distribution in AGN at closer separation.

We note that, as described in the previous section, the bulk of absorption we measure is likely associated with nuclear scale

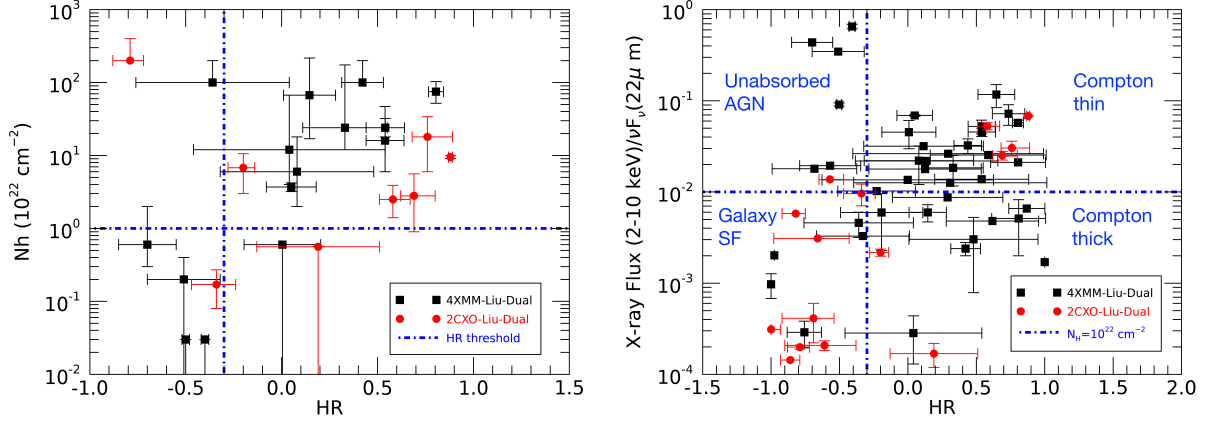


Figure 2. Left: Absorption column density ν s hardness ratio, $HR=(H-S)/(H+S)$ for the clean sample of 24 dual AGN with spectral information (see Table 2). The HR is evaluated considering $S=2\text{--}4.5$ keV and $H=4.5\text{--}10$ keV for 4XMM data, and $S=0.5\text{--}2$ keV and $H=2\text{--}8$ keV for CSC2 data. Dash-dotted vertical line define the threshold for sources with $N_H > 10^{22} \text{ cm}^{-2}$ in our sample. Right: AGN identification and absorption diagnostic using mid-IR ν s HR for the total sample of 42 confirmed dual AGN (see Table 1). Dash-dotted lines identify the regions in the plot where different classes of X-ray and mid-IR emitters are located (Severgnini et al. 2012).

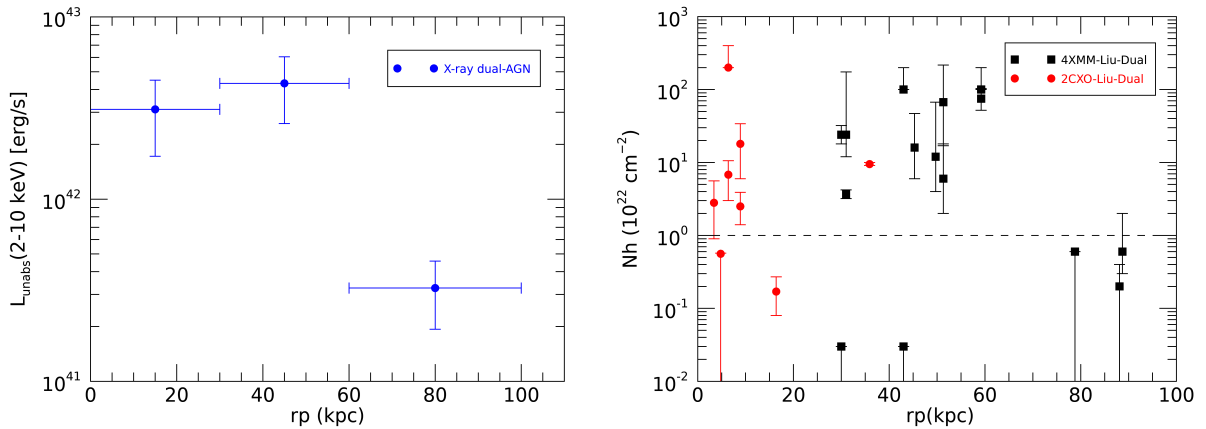


Figure 3. Broad-band intrinsic X-ray luminosity (left) and absorbing column density N_H (right) ν s projected separation r_p for clean sample of X-ray dual AGN detected in 4XMM and CSC2 and with spectral information (see Table 2). L_{unabs} errors are dominated by dispersion in each single bin.

(BLR/torus). This indicates that the observed systems are in environments where gas is transported closer to the AGN and/or disturbed in dual AGN separated by <60 kpc. Based on the data discussed in this work, we find no strong evidence that AGN pairs with projected separations in the $\sim 1\text{--}100$ kpc range prefer gas-rich galaxies (i.e., with a larger fraction of gas mass than other galaxies; Kewley et al. 2006). If confirmed in subsequent observations, this would imply that interactions with gas (via tides, spiral arms, dynamical friction, etc.) are not a necessary mechanism for orbital evolution of AGN pairs from 100 kpc scales. Samples like the one analyzed in this paper could therefore be used to place some initial observational constraints on theoretical models describing orbital evolution of MBH pairs.

5.2 X-ray detection efficiency of dual-AGN candidates

In this section we report the study to evaluate the efficiency of X-ray observations in order to detect optically selected dual-AGN candi-

dates. To this aim, we considered the optically selected sample of AGN pairs and measure the ratio between the number of detected optical AGN and the number of observed optical AGN along the XMM-Newton and Chandra pointings, $X_{\text{eff}} = \text{DET}/\text{OBS}$. To increase the available statistics, in addition to the sample of AGN pairs from Liu et al. 2011, we considered further samples of dual AGN identified from both optical image (Mezcua et al. 2014) and double-peaked emission-line techniques (Ge et al. 2012; Wang et al. 2009; Smith et al. 2010; Kim et al. 2020). The list of the selected samples are reported in table 3. We note that almost 90% of X-ray detected targets in all samples have been observed more than 10 ks of elapsed time. Moreover, most of the detected sources have been observed serendipitously, with an off-axis position up to $12'\text{--}15'$. In order to select the number of observed AGN candidates, we consider here two thresholds: exposure and off-axis position. To take into account the fastest drops of Chandra sensitivity at increasing off-axis angles with respect to XMM-Newton, we selected all targets in the XMM-Newton

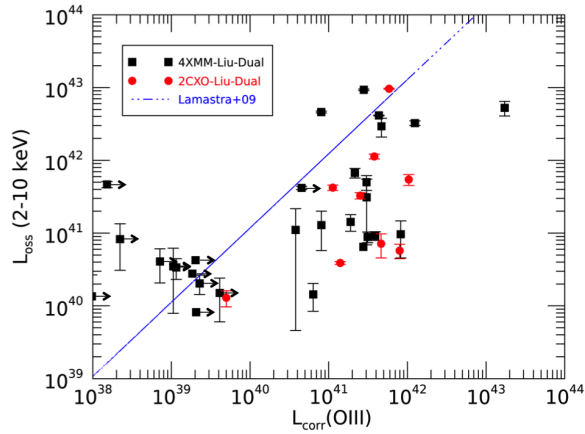


Figure 4. X-ray observed luminosity *vs* de-reddened [OIII] luminosity for the whole sample of confirmed AGN. 4XMM: black squares, CSC2: red dots. Lower limits to $L_{\text{corr}}^{\text{[OIII]}}$ refer to the sources without a measure of $H\beta$ emission, for those we use the observed value of [O III]. The blue dot-dashed line represents the relation found in Lamastra et al. 2009 for a sample of Compton-thick AGN. All sources in pairs lie below the expected relation, suggesting a larger absorption with respect to isolated AGN. The two type 1 AGN in the 4XMM sample are the only measured data points above the relation.

and *Chandra* field of view with an off-axis position lower than $15'$ and $10'$, respectively and with exposure larger than 10 ks. Of course, the number of observed AGN might depend of the threshold we assumed; however, we verified that the number reported below are stable against other choices of off-axis position and exposures close to the selected ones.

In Table 3 we report the ratio X_{eff} of all the optically selected dual AGN detected in 4XMM and CSC2, a row for each optical sample we checked. We stress that these detection fractions should be considered as lower-limits for two main reasons. For what concerns the numerator of the ratio X_{eff} (the X-ray detected optically selected AGN), we note that the upper limit for the undetected sources is in the range 0.004–0.04 cts/s (3σ c.l.) in the 4XMM 2–12 keV band, suggesting that we may fail to detect heavily obscured sources with X-ray luminosity lower than $10^{42} \text{ erg s}^{-1}$, considering an average redshift for our sample of $z=0.03$ and a standard spectral slope of $\Gamma=2$. About the denominator, the X-ray observed optically selected AGN, another important point to consider is the possibility that the optical classification as AGN in the samples under investigation could be instead due SF emission in the galaxy. In fact, as we showed through our MWL analysis (see Sect. 4), about 80% of the optically selected targets are confirmed as AGN. If we consider this fraction, the X-ray detection efficiency considering all optically selected dual AGN in 4XMM and CSC2 (last column in Table 3) is about 60%. Increasing the exposure cut to 15 ks, the detection efficiency weakly increases from 62 to 85%. This suggests that, when observed properly, X-ray data represent a powerful technique to confirm and investigate dual-AGN systems. In this regard, we note that in the sample with higher X-ray detection fraction (Kim et al. 2020, Mezcua et al. 2014 and Ge et al. 2012 for 4XMM, Wang et al. 2009, Smith et al. 2010 and Kim et al. 2020 in the case of *Chandra*), the average value of the off-axis position of the observed targets is lower than in the sample with low X-ray detection efficiency.

6 CONCLUSIONS

We have investigated the properties in the X-ray domain of a sample of optically selected dual AGN with projected separation between 3–97 kpc. Using optical, mid-IR and X-ray diagnostic tools, we were able to characterize the intrinsic properties of this sample and compare them with those of isolated AGN.

- Among 124 X-ray detected dual-AGN candidates, 52 appear in pairs and 72 as single X-ray AGN. We focused our study on AGN selected in pairs, while AGN detected in single sources will be analysed in a forthcoming paper (Parvatikar et al., in preparation).

- Using optical spectroscopy (BPT diagrams in Fig. 1) and X/mid-IR *vs* X-ray HR (Fig. 2), we confirmed as X-ray dual AGN 42 (80%) sources (either LINER or AGN). The X-ray luminosity of LINER sources strongly favours a scenario in which the source emission is accretion-driven. Due to possible identification of heavily obscured AGN with SF (see e.g. case of J133817.3+481632 and J103855.9+392157) and the blended IR emission of unresolved pairs in W4 band, this fraction should be considered as a lower-limit.

- We confirm the trend of increasing AGN luminosity with decreasing separation (see left panel of Fig. 3), suggesting that mergers may trigger more luminous AGN.

- When comparing optical (de-reddened [O III]) and observed X-ray luminosities (i.e., not corrected for the obscuration; see Fig. 4), our sample shows, on average, a larger obscuration with respect to the relation found for obscured Seyfert galaxies in isolated systems. Moreover, systems at closer separation show a higher obscuration with respect to dual AGN with separations r_p above 50–60 kpc.

- The N_{H} measured from X-ray spectral analysis is always higher than the absorbing column density derived from the extinction $E(B-V)$ evaluated for NLR, suggesting that the gas responsible from the obscuration should lie in nuclear regions (likely the torus or BLR).

- Using X/mid-IR ratio *vs* HR (see Fig. 2), we estimate that a fraction of 80% of the confirmed AGN are Compton thin (with N_{H} larger than 10^{22} cm^{-2}) and 16% are Compton thick (N_{H} larger than 10^{24} cm^{-2}). These fractions are larger if compared with samples of isolated systems, but lower with respect to the fraction of heavily obscured AGN found in systems in late-stage of the merging process (projected separation below 10–20 kpc). This evidence is suggesting that pairs of AGN are more heavily obscured with respect to isolated AGN.

- These findings indicate that dual AGN find themselves in environments where gas is transported closer to the AGN and/or disturbed for dual AGN separated by <60 kpc. If the host galaxies of the dual AGN in this sample are further showing to contain similar amounts of gas as galaxies with single AGN, this would suggest that interactions with gas are not a necessary mechanism for orbital evolution of AGN pairs from 100 kpc scales.

- When different samples of dual AGN are considered, we found that the X-ray detection efficiency (defined as the ratio between the X-ray detected and observed optical AGN in dual systems) lies in the range 62–85%, depending on the exposure we considered (10–15 ks, see Table 3). This fraction should be considered as a lower-limit because, due to the limited exposures of X-ray dual systems (mainly observed serendipitously) in 4XMM and CSC2 catalogues, we miss in our analysis all the heavily obscured AGN with 2–10 keV luminosity lower than $10^{42} \text{ erg s}^{-1}$ at $z=0.03$.

Table 3. X-ray detection efficiency of optically selected dual AGN. This is the ratio between the detected optically selected AGN and the observed ones in the field of XMM-Newton and Chandra observations.

Catalogue	⁽¹⁾ Chandra det/obs (%)	⁽¹⁾ XMM det/obs (%)	X-ray tot (%) det/obs (%)
T>10 ks and R _{offset} <15′(XMM)–10′(Chandra)			
Liu et al. 2011	51/137 (37)	73/165 (44)	124/302 (41)
Mezcua et al. 2014	5/16 (31)	7/8 (88)	12/24 (50)
Ge et al. 2012	11/18 (61)	15/17 (88)	26/35 (74)
Wang et al. 2009	8/10 (80)	2/5 (40)	10/15 (67)
Smith et al. 2010	14/17 (82)	6/11 (55)	20/28 (71)
Kim et al. 2020	11/11 (100)	5/6 (83)	16/17 (94)
⁽²⁾ Tot	100/209/0.8 (60)	108/212/0.8 (64)	208/421/0.8 (62)
T>15 ks and R _{offset} <15′(XMM)–10′(Chandra)			
⁽²⁾ Tot	100/154/0.8 (81)	108/152/0.8 (89)	208/306/0.8 (85)

⁽¹⁾ Fraction of AGN detected in 4XMM/CSC2 catalogues over observed with more than 10 ks (upper rows) and 15 ks (last row) considering an off-axis position <10′ for Chandra and <15″ for XMM-Newton. Exposure time refers to elapsed time; ⁽²⁾ The total has been evaluated considering that the number of confirmed AGN is the 80% of the observed targets (see details in Sect. 5.2).

ACKNOWLEDGEMENTS

We would like to thank the referee for the careful reading of the manuscript and useful comments that helped to improve its quality. We acknowledge financial contribution from Bando Ricerca Fondamentale INAF 2022 Large Grant “Dual and binary supermassive black holes in the multi-messenger era: from galaxy mergers to gravitational waves”. ADR, PS, CV, SB acknowledge financial contribution from the agreement ASI-INAF n.2017-14-H.O. MC acknowledges support from NSF AST-200793. This research has made use of data obtained from the 4XMM XMM-Newton serendipitous source catalogue compiled by the 10 institutes of the XMM-Newton Survey Science Centre selected by ESA. This research has made use of data obtained from the Chandra Source Catalog, provided by the Chandra X-ray Center (CXC) as part of the Chandra Data Archive. This publication makes use of data products from the Wide-field Infrared Survey Explorer, which is a joint project of the University of California, Los Angeles, and the Jet Propulsion Laboratory/California Institute of Technology, and NEOWISE, which is a project of the Jet Propulsion Laboratory/California Institute of Technology. WISE and NEOWISE are funded by the National Aeronautics and Space Administration. Funding for SDSS-III has been provided by the Alfred P. Sloan Foundation, the Participating Institutions, the National Science Foundation, and the U.S. Department of Energy Office of Science. The SDSS-III web site is <http://www.sdss3.org/>. SDSS-III is managed by the Astrophysical Research Consortium for the Participating Institutions of the SDSS-III Collaboration including the University of Arizona, the Brazilian Participation Group, Brookhaven National Laboratory, Carnegie Mellon University, University of Florida, the French Participation Group, the German Participation Group, Harvard University, the Instituto de Astrofísica de Canarias, the Michigan State/Notre Dame/JINA Participation Group, Johns Hopkins University, Lawrence Berkeley National Laboratory, Max Planck Institute for Astrophysics, Max Planck Institute for Extraterrestrial Physics, New Mexico State University, New York University, Ohio State University, Pennsylvania State University, University of Portsmouth, Princeton University, the Spanish Participation Group, University of Tokyo, University of Utah, Vanderbilt University, University of Virginia, University of Washington, and Yale University.

DATA AVAILABILITY

The high-level data underlying this article are extracted through standard processing from raw data stored in public archives (SDSS, XMM-Newton, Chandra and WISE), and will be shared on reasonable request to the corresponding author.

REFERENCES

- Alam S., et al., 2015, *ApJS*, **219**, 12
Amaro-Seoane P., et al., 2022, arXiv e-prints, [p. arXiv:2203.06016](https://arxiv.org/abs/2203.06016)
Arnaud K. A., 1996, in Jacoby G. H., Barnes J., eds, *Astronomical Society of the Pacific Conference Series Vol. 101, Astronomical Data Analysis Software and Systems V*. p. 17
Assef R. J., et al., 2013, *ApJ*, **772**, 26
Ballo L., Braito V., Della Ceca R., Maraschi L., Tavecchio F., Dadina M., 2004, *ApJ*, **600**, 634
Balucinska-Church M., McCammon D., 1992, *ApJ*, **400**, 699
Bassani L., Dadina M., Maiolino R., Salvati M., Risaliti G., Della Ceca R., Matt G., Zamorani G., 1999, *ApJS*, **121**, 473
Bianchi S., Chiaberge M., Piconcelli E., Guainazzi M., Matt G., 2008, *MNRAS*, **386**, 105
Bianchi S., Guainazzi M., Laor A., Stern J., Behar E., 2019, *MNRAS*, **485**, 416
Blecha L., Snyder G. F., Satyapal S., Ellison S. L., 2018, *MNRAS*, **478**, 3056
Burke-Spolaor S., 2011, *MNRAS*, **410**, 2113
Calderone G., Nicastro L., Ghisellini G., Dotti M., Sbarro T., Shankar F., Colpi M., 2017, *MNRAS*, **472**, 4051
Capelo P. R., Dotti M., Volonteri M., Mayer L., Bellovary J. M., Shen S., 2017, *MNRAS*, **469**, 4437
Cardelli J. A., Clayton G. C., Mathis J. S., 1989, *ApJ*, **345**, 245
Cash W., 1979, *ApJ*, **228**, 939
Comerford J. M., Gerke B. F., Stern D., Cooper M. C., Weiner B. J., Newman J. A., Madsen K., Barrows R. S., 2012, *ApJ*, **753**, 42
De Rosa A., et al., 2015, *MNRAS*, **453**, 214
De Rosa A., et al., 2018, *MNRAS*, **480**, 1639
De Rosa A., et al., 2019, *New Astron. Rev.*, **86**, 101525
Di Matteo T., Springel V., Hernquist L., 2005, *Nature*, **433**, 604
Domínguez A., et al., 2013, *ApJ*, **763**, 145
Draine B. T., 2011, *Physics of the Interstellar and Intergalactic Medium*
Evans I. N., et al., 2010, *ApJS*, **189**, 37
Evans I. N., et al., 2020, in *American Astronomical Society Meeting Abstracts* #235. p. 154.05

- Foord A., Gültekin K., Nevin R., Comerford J. M., Hodges-Kluck E., Barrows R. S., Goulding A. D., Greene J. E., 2020, *ApJ*, **892**, 29
- Fu H., Myers A. D., Djorgovski S. G., Yan L., Wrobel J. M., Stockton A., 2015, *ApJ*, **799**, 72
- Ge J.-Q., Hu C., Wang J.-M., Bai J.-M., Zhang S., 2012, *ApJS*, **201**, 31
- González-Martín O., Masegosa J., Márquez I., Guainazzi M., Jiménez-Bailón E., 2009, *A&A*, **506**, 1107
- Guainazzi M., Piconcelli E., Jiménez-Bailón E., Matt G., 2005, *A&A*, **429**, L9
- Guainazzi M., et al., 2021, *MNRAS*, **504**, 393
- HI4PI Collaboration et al., 2016, *A&A*, **594**, A116
- Haardt F., Maraschi L., 1993, *ApJ*, **413**, 507
- Haardt F., Maraschi L., Ghisellini G., 1994, *ApJ*, **432**, L95
- Heckman T. M., 1980, *A&A*, **87**, 152
- Heckman T. M., Ptak A., Hornschemeier A., Kauffmann G., 2005, *ApJ*, **634**, 161
- Ho L. C., Filippenko A. V., Sargent W. L. W., 1993, *ApJ*, **417**, 63
- Hopkins P. F., Hernquist L., Cox T. J., Di Matteo T., Robertson B., Springel V., 2006, *ApJS*, **163**, 1
- Hou M., Liu X., Guo H., Li Z., Shen Y., Green P. J., 2019, *ApJ*, **882**, 41
- Hou M., Li Z., Liu X., 2020, *ApJ*, **900**, 79
- Husemann B., Heidt J., De Rosa A., Vignali C., Bianchi S., Bogdanović T., Komossa S., Paragi Z., 2020, *A&A*, **639**, A117
- Iwasawa K., et al., 2011, *A&A*, **529**, A106
- Iwasawa K., et al., 2020, *A&A*, **640**, A95
- Jarrett T. H., et al., 2011, *ApJ*, **735**, 112
- Kauffmann G., et al., 2003, *MNRAS*, **346**, 1055
- Kewley L. J., Groves B., Kauffmann G., Heckman T., 2006, *MNRAS*, **372**, 961
- Kim D. C., Yoon I., Evans A. S., Kim M., Momjian E., Kim J. H., 2020, *ApJ*, **904**, 23
- Kocevski D. D., et al., 2012, *ApJ*, **744**, 148
- Kocevski D. D., et al., 2015, *ApJ*, **814**, 104
- Komossa S., Böhringer H., Huchra J. P., 1999, *A&A*, **349**, 88
- Komossa S., Burwitz V., Hasinger G., Predehl P., Kaastra J. S., Ikebe Y., 2003, *ApJ*, **582**, L15
- Koss M., Mushotzky R., Veilleux S., Winter L., 2010, *ApJ*, **716**, L125
- Koss M., et al., 2011, *ApJ*, **735**, L42
- Koss M., Mushotzky R., Treister E., Veilleux S., Vasudevan R., Trippie M., 2012, *ApJ*, **746**, L22
- Lamastra A., Bianchi S., Matt G., Perola G. C., Barcons X., Carrera F. J., 2009, *A&A*, **504**, 73
- Liu X., Shen Y., Strauss M. A., Hao L., 2011, *ApJ*, **737**, 101
- Mannucci F., et al., 2022, *Nature Astronomy*,
- Marinucci A., Bianchi S., Nicastro F., Matt G., Goulding A. D., 2012, *ApJ*, **748**, 130
- Mateos S., et al., 2012, *MNRAS*, **426**, 3271
- Mazzarella J. M., et al., 2012, *AJ*, **144**, 125
- Mezcua M., Lobanov A. P., Mediavilla E., Karouzos M., 2014, *ApJ*, **784**, 16
- Mulchaey J. S., Koratkar A., Ward M. J., Wilson A. S., Whittle M., Antonucci R. R. J., Kinney A. L., Hurt T., 1994, *ApJ*, **436**, 586
- Osterbrock D. E., Ferland G. J., 2006, *Astrophysics of gaseous nebulae and active galactic nuclei*
- Padovani P., et al., 2017, *A&ARv*, **25**, 2
- Pfeifle R. W., et al., 2019, *ApJ*, **875**, 117
- Piconcelli E., et al., 2010, *ApJ*, **722**, L147
- Ranalli P., Comastri A., Setti G., 2003, *A&A*, **399**, 39
- Ricci C., Ueda Y., Koss M. J., Trakhtenbrot B., Bauer F. E., Gandhi P., 2015, *ApJ*, **815**, L13
- Ricci C., et al., 2017, *MNRAS*, **468**, 1273
- Ricci C., et al., 2021, *MNRAS*, **506**, 5935
- Satyapal S., Ellison S. L., McAlpine W., Hickox R. C., Patton D. R., Mendel J. T., 2014, *MNRAS*, **441**, 1297
- Satyapal S., et al., 2017, *ApJ*, **848**, 126
- Severgnini P., Caccianiga A., Della Ceca R., 2012, *A&A*, **542**, A46
- Shields J. C., 1992, *ApJ*, **399**, L27
- Silverman J. D., et al., 2011, *ApJ*, **743**, 2
- Smith K. L., Shields G. A., Bonning E. W., McMullen C. C., Rosario D. J., Salviander S., 2010, *ApJ*, **716**, 866
- Terashima Y., Hirata Y., Awaki H., Oyabu S., Gandhi P., Toba Y., Matsuhara H., 2015, *ApJ*, **814**, 11
- Torres-Albà N., et al., 2018, *A&A*, **620**, A140
- Treister E., Schawinski K., Urry C. M., Simmons B. D., 2012, *ApJ*, **758**, L39
- Ueda Y., et al., 2007, *ApJ*, **664**, L79
- Vignali C., Alexander D. M., Gilli R., Pozzi F., 2010, *MNRAS*, **404**, 48
- Volonteri M., Pfister H., Beckmann R., Dotti M., Dubois Y., Massonneau W., Musoke G., Tremmel M., 2022, *MNRAS*, **514**, 640
- Wachter K., Leach R., Kellogg E., 1979, *ApJ*, **230**, 274
- Wang J.-M., Chen Y.-M., Hu C., Mao W.-M., Zhang S., Bian W.-H., 2009, *ApJ*, **705**, L76
- Webb N. A., et al., 2020, *A&A*, **641**, A136
- Weston M. E., McIntosh D. H., Brodwin M., Mann J., Cooper A., McConnell A., Nielsen J. L., 2017, *MNRAS*, **464**, 3882
- Wright E. L., et al., 2010, *AJ*, **140**, 1868
- Yan L., et al., 2013, *AJ*, **145**, 55

This paper has been typeset from a \LaTeX file prepared by the author.